Enhanced Spin-Orbit Torque Induced by Interfacial Scattering in Ir/Pt Superlattice

Jiahui Li[1,2†], Jing Dong[3†], Yuqiang Wang[1†], Mingtong Zhu[1,4], Yang Yao[5], Ying Meng[1,4], Jiyang Ou[1,2], Guibin Lan[1,2], Xuming Luo[1,2], Jihao Xia[1,2], Hongjun Xu[1], Yizhan Wang[1,2], Jiafeng Feng[1,2], Hongxiang Wei[1], Congli He[6], Richeng Yu[1,3,4], Junwei Zhang[5], Yong Peng[5], Nianpeng Lu[1,4], Caihua Wan[1], Xiufeng Han[1,2], and Guoqiang Yu[1,2*]

[1]*Beijing National Laboratory for Condensed Matter Physics, Institute of Physics, Chinese Academy of Sciences, Beijing 100190, China*
[2]*Center of Materials Science and Optoelectronics Engineering, University of ChineseAcademy of Sciences, Beijing 100049, China*
[3]*Songshan Lake Materials Laboratory, Dongguan 523808, China*
[4]*School of Physical Sciences, University of Chinese Academy of Sciences, Beijing 100049, China*
[5]*Electron Microscopy Centre of Lanzhou Universityand Electron Microscopy Centre of Lanzhou University, Lanzhou 730000, China*
[6]*School of Physics and Astronomy, Beijing Normal University, Beijing 100875, China*

(Received 27 February 2025; accepted manuscript online 1 April 2025)

The mechanisms of enhancing spin-orbit torque (SOT) have attracted significant attention, particularly regarding the influence of extrinsic scattering mechanisms on SOT efficiency, as they complement intrinsic contributions. In multilayer systems, extrinsic interfacial scattering, along with scattering from defects or impurities inside the materials, plays a crucial role in affecting the SOT efficiency. In this study, we successfully fabricated high-quality epitaxially grown $[Ir/Pt]_N$ superlattices with an increasing number of interfaces using a magnetron sputtering system to investigate the contribution of extrinsic interfacial scattering to SOT efficiency. We measured SOT efficiency through spin-torque ferromagnetic resonance methods and determined the spin Hall angle using the spin pumping technique. Additionally, we calculated spin transparency based on the SOT efficiency and spin Hall angle. Our findings indicate that the values of SOT efficiency, spin Hall angle, and spin transparency are enhanced in the superlattice structure compared to Pt, which we attribute to the increase in interfacial scattering. This research offers an effective strategy for designing and fabricating advanced spintronic devices.

DOI: 10.1088/0256-307X/42/5/057401 CSTR: 32039.14.0256-307X.42.5.057401

Introduction. Spin-orbit torque (SOT), arising from the interplay between magnetization and spin currents induced by effects such as the spin Hall effect (SHE),[1–6] the Rashba effect,[7] and other current-spin conversion mechanisms, has garnered significant attention in recent decades. This phenomenon enables the manipulation of magnetic moments, including magnetization switching,[8–10] domain wall motion,[11,12] and the dynamics of skyrmion.[13–16] As a critical element in the development of spintronic devices, such as memory devices,[17–19] logic devices,[20–22] and magnetic oscillators,[23–26] understanding and enhancing SOT efficiency is vital for reducing energy consumption and Joule heating in practical applications. Consequently, investigating strategies to improve SOT efficiency is essential for realizing energy-efficient spintronic technologies. Several approaches have been proposed to boost SOT efficiency, including the use of heavy metals with large intrinsic spin Hall angles θ_{SH} (SHA) driven by Berry curvature,[27] as well as the introduction of defects and impurities to increase the contributions of extrinsic skew-scattering and side-jump scattering mechanisms.[28–32] Additionally, leveraging the spin-momentum locking effect of topological insulators[33–37] and topological semimetals[38–41] presents promising avenues for the SOT enhancement.

Heavy metals such as Pt, Ta, and W,[42–44] have garnered significant interest for SOT applications due to their low resistivity, effectively mitigating ohmic loss. Pt has emerged as a focal point among these materials due to its low resistivity and notable SOT efficiency.[45–48] However, despite its superior conductivity, the SOT efficiency of Pt is lower than that of Ta and W, underscoring the necessity to enhance the SOT performance of Pt. The SHE plays a critical role in determining SOT efficiency, with contributions from both intrinsic properties, primarily driven by Berry curvature, and extrinsic factors related to scattering events involving impurities and defects. Traditionally, defects and impurities have been utilized to enhance scattering, thereby improving SOT efficiency.[18,28–31] Moreover, understanding the role of interfacial scattering is crucial,

†These authors contributed equally to this work.
*Corresponding author. Email: guoqiangyu@iphy.ac.cn
© 2025 Chinese Physical Society and IOP Publishing Ltd. All rights, including for text and data mining, AI training, and similar technologies, are reserved.

as it significantly impacts both resistivity [49–51] and spin relaxation. [52] To examine the effects of interfacial scattering on SOT, it is essential for the spin source layer to exhibit high crystalline quality, thereby minimizing the extrinsic scattering from inherent defects and impurities and highlighting the impact of the interfaces.

In this study, we constructed an epitaxially grown $[Ir/Pt]_N$ superlattice system characterized by a high-quality crystalline structure aimed at minimizing extrinsic scattering. The choice of Ir as a constituent material is motivated by its excellent lattice compatibility with Pt. Both materials share the same space group ($Fm\bar{3}m$) and possess similar lattice constants, which minimize structural mismatch. We use spin-torque ferromagnetic resonance (ST-FMR) and spin-pumping (SP) techniques to quantify SOT efficiency, SHA, and spin transparency. Our findings reveal that interfacial scattering plays a significant role in enhancing these three parameters, providing valuable insights for developing advanced spintronic devices.

Experiments and Results. Samples with the structure $[Ir(t)/Pt(t)]_N$ were deposited by magnetron sputtering, where $2t \times N = 12$ nm and $N = 3$, 4, 5, and 6. α-Al_2O_3(0001) substrates were used to ensure epitaxial growth between the substrate and the sample. Initially, the α-Al_2O_3(0001) substrates were heated to 800 ℃ and maintained at this temperature for 30 minutes to degas and achieve a clean surface. Subsequently, Pt and Ir layers were deposited to form a (111) structure while maintaining the substrate at an elevated temperature. After deposition, the samples underwent *in situ* annealing at 800 ℃ for 1 hour to enhance their crystalline quality.

Figure 1(a) shows the θ–2θ results of Pt, Ir, and Ir/Pt superlatticeas measured by X-ray diffraction (XRD). The peaks corresponding to the (111) planes of Pt and Ir layers are at $2\theta = 39.5°$ and 40.6°, respectively. Utilizing the Bragg equation ($2d\sin\theta = \lambda$), where d is the interplanar spacing, and λ is the X-ray wavelength (1.5406 Å), the (111) interplanar spacings for Pt and Ir can be calculated as 2.279 nm and 2.219 nm, respectively. The presence of Laue oscillations alongside the main peak further confirms the high crystalline quality of the sample. As shown in Fig. S1(a), a wider angular range in the XRD θ–2θ scan reveals that both Pt and Ir exhibit a well-defined out-of-plane single (111) orientation, demonstrating successful epitaxial growth with high crystallinity along the normal direction of the substrate. Figures S1(b) and S1(c) show the in-plane alignment of the Pt and Ir layers using φ-scan. For a Pt (111) film with a single domain, the {220} planes should display a 3-fold symmetry. However, in our case, the Pt (111) deposited on α-Al_2O_3 (0001) exhibits a 6-fold symmetry, indicating the presence of two domains with a 60° angular deviation. This phenomenon has been reported in previous studies. [53,54] Similar behavior was also observed in the Ir films.

Table 1. Angular positions of the main and satellite peaks with various diffraction orders ($N = 3$, 4, 5, and 6).

Periods	Order				
	0	−2	−1	1	2
$N = 3$	40.04°	35.38°	37.70°	42.40°	44.84°
$N = 4$	40.04°	33.84°	36.93°	43.19°	46.37°
$N = 5$	40.04°	32.31°	36.15°	43.98°	47.97°
$N = 6$	40.04°	30.78°	35.38°	44.77°	49.59°

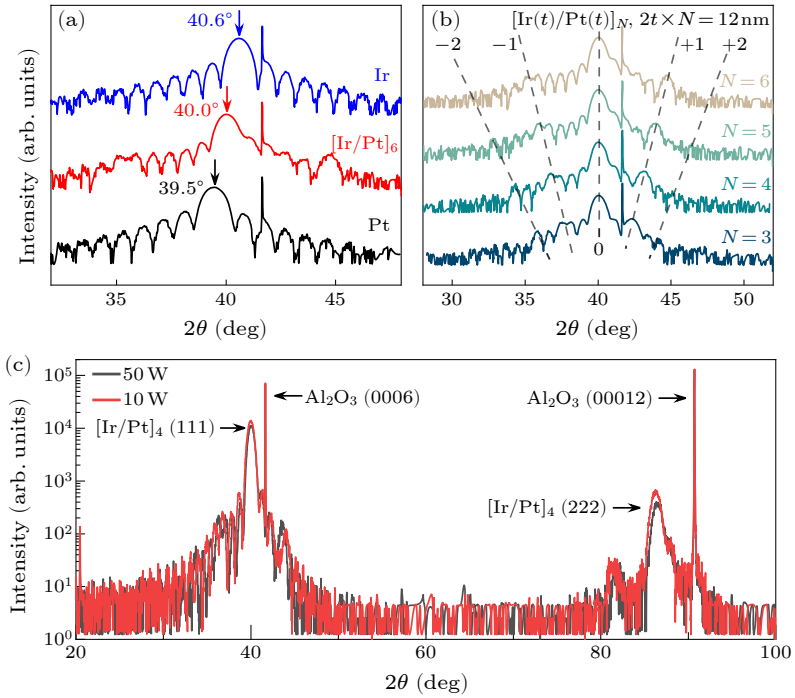

Fig. 1. XRD θ–2θ measurements of the superlattice samples. (a) Comparison of θ–2θ scan for the (111) diffraction peaks of Pt, Ir, and the $[Ir/Pt]_6$ superlattices. The thicknesses of Pt and Ir are both 10 nm, while the total thickness of the $[Ir/Pt]_6$ superlattice is 12 nm. (b) Variation of satellite peak positions of the superlattices as a function of the number of periods. (c) XRD θ–2θ patterns of the $[Ir/Pt]_4$ superlattices deposited under different conditions, measured over a broader angular range ($20° \le 2\theta \le 100°$). The total thickness of the $[Ir/Pt]_4$ superlattice is 10.8 nm.

Subsequently, XRD θ–2θ measurements were conducted on the $[\mathrm{Ir}(t)/\mathrm{Pt}(t)]_N$ samples. Figure 1(b) shows the XRD θ–2θ results for the superlattice. The positions of the main peak and satellite peaks can also be calculated using the formula $2h \times |\sin\theta_n - \sin\theta_m| = |n - m|\lambda$, where h is the thickness of each period of the superlattice, and n and m denote the orders corresponding to the satellite peaks. The XRD measurements shown in Fig. 1(b) align well with the calculated results presented in Table 1. To enhance the crystallization of the samples, two deposition conditions with significantly different deposition rates were employed, 10 W with 20 mTorr of Ar pressure and 50 W with 3 mTorr of Ar pressure, aiming to achieve higher-quality superlattices. Specifically, under the condition of 10 W with 20 mTorr, the deposition rates of Pt and Ir are 0.051 Å/s and 0.049 Å/s, respectively. Under the condition of 50 W with 3 mTorr, the deposition rates of Pt and Ir are 0.535 Å/s and 0.370 Å/s, respectively. The XRD θ–2θ spectra of these two samples are shown in Fig. 1(c). Both samples exhibit peaks corresponding to the (111) planes. However, the intensity of the sample prepared at 10 W with 20 mTorr (red line) is approximately 25% higher than that of the sample prepared at 50 W with 3 mTorr (black line). This observation proves that the crystalline quality of the samples prepared under the lower power condition (10 W with 20 mTorr) is superior. Further evidence supporting this conclusion is presented in Figs. S1(d) and S1(e). Although both samples exhibit narrow full-width at half-maximum (FWHM) values in their rocking curves, the sample prepared under the low-power condition demonstrates a narrower FWHM, indicating optimized crystalline quality.

Scanning transmission electron microscopy (STEM) analyses were performed to further elucidate the differences between the two samples. Figures 2(a) and 2(e) display high-angle annular dark field (HAADF) images of Pt and Ir films, respectively, where clear crystallization is observed. The fast Fourier transform (FFT) images corresponding to Figs. 2(a) and 2(e) are presented in Figs. S2(a) and S2(b). Pt and Ir exhibit only a sharp, single set of lattice points in reciprocal space. Figures 2(b) and 2(f) show the HAADF images of the samples deposited under different growth conditions, revealing minimal difference between them. However, the FFT reciprocal space images of the 50 W sample exhibit additional scattered points [labeled by the dashed lines in Fig. 2(g)] compared to those of the sample grown at 10 W [see Figs. 2(c) and 2(g)]. This observation indicates that the crystalline quality of the sample prepared at 10 W with 20 mTorr is superior to that of the sample grown at 50 W with 3 mTorr. Figures 2(d) and 2(h) present the energy dispersive spectroscopy (EDS) mappings of these two samples, respectively. The elemental layers are distinctly defined, and the interfaces between layers confirm the formation of the superlattice, with no significant elemental diffusion occurring even at 800 ℃.

To study the SOT effect induced by the superlattices, a series of samples was prepared with the structure [Ir (k layers)/Pt (k layers)]$_N$/NiFe (8 nm)/MgO (2 nm)/Ta (1.5 nm), where N is the number of periods ($N = 2$, 3, 4, and 6) and k is the number of atom layers. To ensure a uniform thickness across the superlattices, $k \times N$ is selected as the common multiple of the period number, i.e., $k \times N = 24$, and the total thickness of the superlattices is 10.8 nm. For comparison, samples with the structures of Pt (10.8 nm)/NiFe (8 nm)/MgO (2 nm)/Ta (1.5 nm) and Ir (10.8 nm)/NiFe (8 nm)/MgO (2 nm)/Ta (1.5 nm) were also deposited, with the thickness of Pt or Ir being consistent with that of the superlattice samples. After depositing the superlattices under the conditions above, the magnetic layer and capping layers NiFe (8 nm)/MgO (2 nm)/Ta (1.5 nm) were subsequently deposited after the samples had cooled to room temperature. To confirm that the superlattice structure remained intact following the deposition of NiFe (8 nm)/MgO (2 nm)/Ta (1.5 nm), XRD θ–2θ scans were conducted, as shown in Fig. S1(f). The results indicate that not only do the peaks of the superlattice remain present, but the NiFe also exhibits a distinct (111) texture influenced by the underlying superlattice structure.

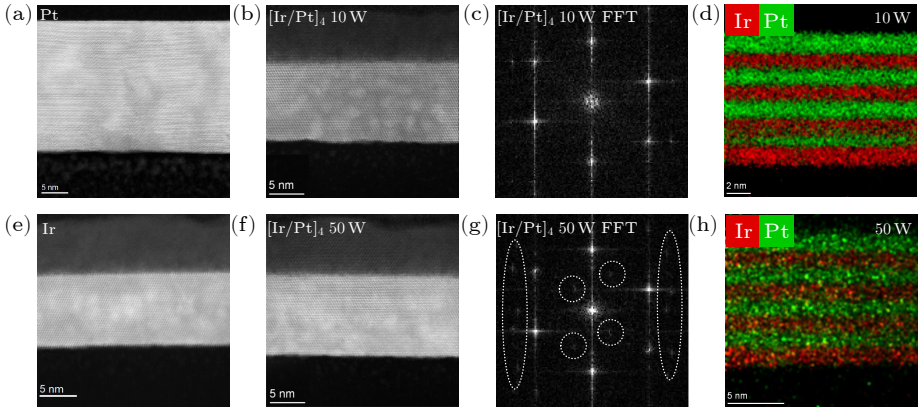

Fig. 2. Scanning transmission electron microscopy (STEM) analyses of Pt, Ir, and $[\mathrm{Ir/Pt}]_4$. (a) and (e) High-angle annular dark field (HAADF) images of Pt and Ir, respectively. (b) and (f) HAADF images of the $[\mathrm{Ir/Pt}]_4$ superlattice deposited under different conditions. (c) and (g) Fast Fourier transform images of (b) and (f), respectively. The dashed lines label the additional scattered points compared to (c). (d) and (h) The EDS mappings of the samples in (c) and (g), respectively.

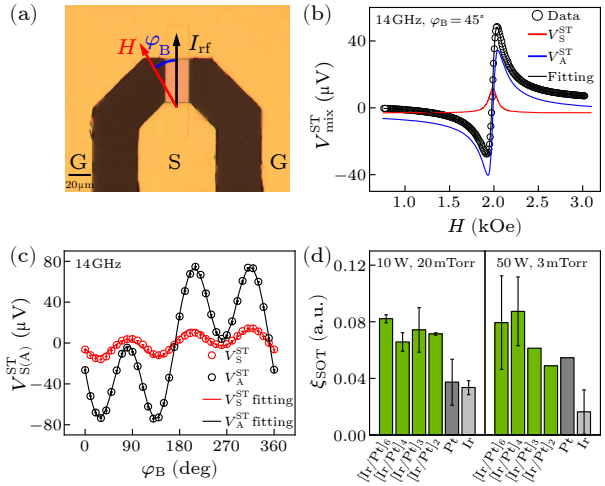

Fig. 3. Spin torque ferromagnetic resonance measurement of the superlattice samples. (a) Optical microscopy image of the ST-FMR device. (b) Typical $V_{\rm mix}^{\rm ST}$ as a function of H and the corresponding fitting curves for the [Ir (4 layers)/Pt (4 layers)]$_6$/NiFe (8 nm)/MgO (2 nm)/Ta (1.5 nm) sample. The frequency of the microwave is 14 GHz, and $\varphi_{\rm B}$ is 45°. (c) Angular dependence of $V_{\rm S(A)}^{\rm ST}$ and the fitting curves at 14 GHz for the sample shown in (b). (d) Comparative summary of the measured SOT efficiency for the two series of samples.

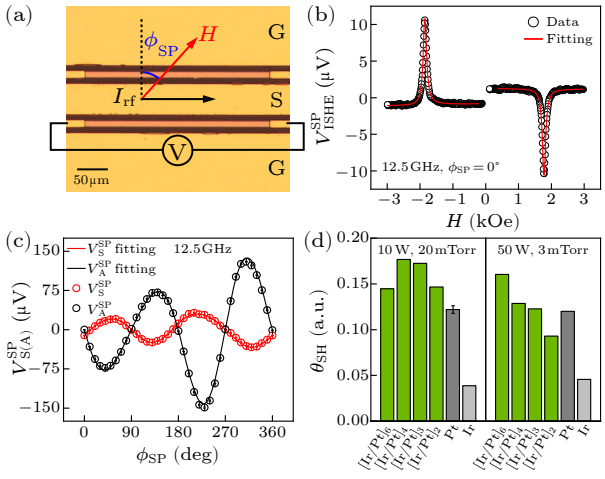

Fig. 4. Spin pumping measurement of the superlattice samples. (a) Optical microscopy image of the SP device. (b) Typical measured $V_{\rm ISHE}^{\rm SP}$ as a function of H and the corresponding fitting curves for the sample with a structure of [Ir (4 layers)/Pt (4 layers)]$_6$/NiFe (8 nm)/MgO (2 nm)/Ta (1.5 nm). The microwave has a frequency of 12.5 GHz, and $\phi_{\rm SP}$ is 0°. (c) Angular dependence of $V_{\rm S(A)}^{\rm SP}$ and the fitting curve for the sample in (b). (d) Comparative summary of estimated spin Hall angles for the two series of samples.

Next, to characterize the SOT induced by the superlattice, we fabricated an ST-FMR device and measured the SOT efficiency using the ST-FMR technique.[40,45,55] Figure 3(a) shows a typical photo and the measurement configuration of ST-FMR devices. $\varphi_{\rm B}$ is the angle between the microwave current $I_{\rm rf}$ and the external magnetic field H. Microwave current is injected into the ground-source-ground (GSG) electrode, and a rectification voltage ($V_{\rm mix}^{\rm ST}$) can be detected. Figure 3(b) shows the typical data and fitting curves, where the data can be fitted by

$$V_{\rm mix}^{\rm ST} = \frac{V_{\rm S}^{\rm ST}\cdot\Delta H^2 + V_{\rm A}^{\rm ST}\cdot\Delta H(H-H_0)}{(H-H_0)^2+\Delta H^2}. \quad (1)$$

Here, $V_{\rm S}^{\rm ST}$ and $V_{\rm A}^{\rm ST}$ are the amplitudes of symmetric and antisymmetric components, respectively, ΔH is the FMR linewidth, and H_0 is the resonance field. Based on the relationship $V_{\rm S(A)}^{\rm ST}(\varphi_{\rm B}) = V_{\rm S(A)}^{0}\sin 2\varphi_{\rm B}\cos\varphi_{\rm B}$, the amplitude $V_{\rm S(A)}^{\rm ST}$ can be obtained by fitting the angular dependence data presented in Fig. 3(c). Furthermore, the SOT efficiency $\xi_{\rm SOT}$ can be calculated using the following equation:

$$\xi_{\rm SOT} = \frac{V_{\rm S}^{0}}{V_{\rm A}^{0}}\cdot\left(\frac{e\mu_0 M_{\rm S} t_{\rm F} t_{\rm H}}{\hbar}\right)\cdot\sqrt{1+\frac{4\pi M_{\rm eff}}{H_0}}, \quad (2)$$

where $M_{\rm S}$ is the saturation magnetization, $t_{\rm F}$ and $t_{\rm H}$ are the thicknesses of the NiFe and Ir/Pt superlattice, respectively. $M_{\rm eff}$ is the effective magnetization, which can be obtained by fitting the Kittel equation to the data, as shown in Fig. S3(a). Figure 3(d) summarizes the $\xi_{\rm SOT}$ values for all samples. The $\xi_{\rm SOT}$ of Pt prepared under 10 W and 20 mTorr is 0.037, which is consistent with previous studies on the epitaxial Pt.[56] The $\xi_{\rm SOT}$ of epitaxial Pt is lower than that of polycrystalline Pt,[57] which is due to the reduced contribution from extrinsic scattering induced by defects and impurities. In contrast, the $\xi_{\rm SOT}$ of the superlattice samples demonstrates a general enhancement compared to the Pt. Under the conditions of 10 W and 20 mTorr, the maximum and average $\xi_{\rm SOT}$ values for the superlattices show enhancements of 120% and 96.4% compared to Pt deposited under the same conditions, respectively. At the elevated power of 50 W with 3 mTorr, the corresponding maximum and average $\xi_{\rm SOT}$ values for the superlattice show enhancements of 60.4% and 27.1% compared to Pt at the same power and pressure, respectively.

Given that the field-like torque ($\xi_{\rm FL}$) is significantly weak and the damping-like torque ($\xi_{\rm DL}$) dominates in this system,[55,56] it is reasonable to consider that $\xi_{\rm SOT} \approx \xi_{\rm DL} = T_{\rm int}\cdot\theta_{\rm SH}$, where $T_{\rm int}$ is the spin transparency. To investigate the enhancement mechanism of $\xi_{\rm SOT}$ in the superlattice, we first extract the $\theta_{\rm SH}$ through the SP measurement. A typical SP device is shown in Fig. 4(a). Microwaves are introduced into the GSG electrodes to generate an Oersted field in microwave frequency, and a stripe with 300 μm in length and 8 μm in width is placed in the gap of the GSG. The ferromagnetic layer's precession, driven by the microwave field, generates spin current via the SP effect, which then diffuses into the heavy metal layer to produce an inverse spin Hall effect (ISHE) voltage $V_{\rm ISHE}^{\rm SP}$. This voltage can be detected by the electrodes connected to the stripe. $\phi_{\rm SP}$ is the angle between the perpendicular direction of the microwave current and the external field H. When H is perpendicular to the stripe, i.e., $\phi_{\rm SP} = 0$, the pure ISHE signal can be detected. A typical ISHE voltage produces a symmetric Lorentz curve, as shown in Fig. 4(b), where the microwave frequency is

12.5 GHz. It can be fitted by

$$V_{\mathrm{ISHE}}^{\mathrm{SP}}(H) = \lambda\theta_{\mathrm{SH}}\tanh\left(\frac{t_N}{2\lambda}\right)\frac{\hbar}{e}\omega G_{\mathrm{eff}}^{\uparrow\downarrow} wR|\alpha||\beta| \cdot \frac{\Delta H^2}{(H-H_0)^2+\Delta H^2}. \quad (3)$$

Here, $\hbar$ is the reduced Planck constant, e is the electron charge, λ is the spin diffusion length, t_N is the thickness of the superlattice, w is the width of the stripe, R is the resistance of the stripe, ω is the angular frequency, $G_{\mathrm{eff}}^{\uparrow\downarrow}$ is the effective spin mixing conductance, α and β are the amplitudes of the in-plane and out-of-plane precession angles, respectively. M_{eff} is the effective magnetization obtained using the Kittel equation in Fig. S4(a).

Considering the significant spin rectification effects in this system, we also measured the angular dependence of the voltage to obtain the exact value of $V_{\mathrm{ISHE}}^{\mathrm{SP}}$, as shown in Fig. 4(c). The angular dependent data can be fitted by

$$V_{\mathrm{A}}^{\mathrm{SP}} = V_{\mathrm{AI}}\sin^2\varphi\cos\varphi + V_{\mathrm{AO}}\sin 2\varphi,$$
$$V_{\mathrm{S}}^{\mathrm{SP}} = V_{\mathrm{SI}}\sin^2\varphi\cos\varphi + V_{\mathrm{SO}}\sin 2\varphi + V_{\mathrm{ISHE}}^{\mathrm{SP}}\cos\varphi. \quad (4)$$

Here, V_{AI} (V_{AO}) and V_{SI} (V_{SO}) are the coefficients of spin rectification voltages due to the in-plane and out-of-plane microwave magnetic fields. The SP results for these samples are summarized in Fig. 4(d). Given the similar spin diffusion lengths of Pt and Ir,[57,58] the superlattices can be approximately regarded as a single layer with a 1.25 nm spin diffusion length to simplify calculations.[57,58] It is evident that the θ_{SH} values of the superlattice samples, regardless of growth conditions, are generally greater than those of the Pt reference sample. Under the conditions of 10 W and 20 mTorr, the maximum and average θ_{SH} values for the superlattice show enhancements of 44.8% and 31.2% compared to Pt deposited at 10 W, respectively. At the higher power of 50 W with 3 mTorr, the corresponding maximum and average θ_{SH} values for the superlattice show enhancements of 33.7% and 5.2% compared to Pt deposited at 50 W, respectively. This improvement can be attributed to the enhanced extrinsic mechanism resulting from additional interfacial scattering in the superlattice.

Moreover, the results from ST-FMR and SP indicate light differences in the trends of ξ_{SOT} and θ_{SH}. This implies that T_{int} is also influenced by the interfacial scattering because of $T_{\mathrm{int}} = \xi_{\mathrm{SOT}}/\theta_{\mathrm{SH}}$. Figures 5(a) and 5(b) show the T_{int} values obtained experimentally (shown in black). Notably, the T_{int} of the superlattices shows a general enhancement compared to that of Pt. To elucidate the origin of this enhancement, we also calculated T_{int} using the equation:[46] $T_{\mathrm{int}} = 2G_{\mathrm{eff}}^{\uparrow\downarrow}/G_{\mathrm{NM}}$.

$$G_{\mathrm{eff}}^{\uparrow\downarrow} = \frac{e^2}{\hbar}\cdot\frac{4\pi M_{\mathrm{S}} t_{\mathrm{F}}}{g\mu_{\mathrm{B}}}(\alpha-\alpha_{\mathrm{F}}),$$
$$G_{\mathrm{NM}} = \frac{1}{\rho\lambda},$$

where g, ρ, μ_{B}, α, and α_{F} represent Landég-factor, conductivity, Bohr magneton, damping of the (Pt, Ir, or multilayers)/NiFe, and the damping of NiFe itself, respectively. The values of α were determined through linear fitting of ΔH with f, as shown in Fig. S4(b). In this equation, the primary variable is the resistivity of the superlattices. Consequently, we measured the resistances of both series of samples for further calculations, as shown in Fig. 5(c). The estimated T_{int} values, represented by the red data points, exhibit a trend similar to the experimental results. The parameters used in the calculations are with $g = 2$, $t_{\mathrm{F}} = 8$ nm, M_{S} ranges from 946 to 973 emu/cc, and α ranges from 0.011 to 0.012, where M_{S} and α were extracted from fits to data obtained from various samples. The consistency between the experiments and calculations further supports that the experimental findings can be understood based on the equation of T_{int}. Subsequently, we fit the spin Hall conductivity $\rho_{\mathrm{SH}} = k^{\mathrm{sk}}\Delta\rho + k^{\mathrm{sj}}\Delta\rho^2$ to determine the extrinsic mechanism, where $\rho_{\mathrm{SH}} \approx \theta_{\mathrm{SH}}\cdot\rho$, k^{sk} and k^{sj} are contribution factors of skew scattering and side jump scattering. $\Delta\rho = \rho - \rho_0$ can be calculated using data in Fig. 5(c), and ρ_0 is the resistivity calculated without considering interfacial scattering of $[\mathrm{Ir/Pt}]_N$. Figure S5 shows the fitting curve of ρ_{SH}, the values of k^{sk} and k^{sj} are 0.142 and 0.007, respectively. These results suggest that skew scattering plays a dominant role in improving SOT efficiency.

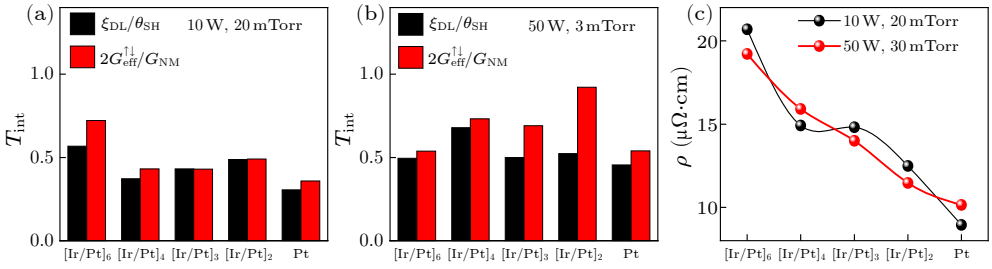

Fig. 5. Calculated results of transparency using two methods. (a) and (b) Comparison of transparency at the superlattice/NiFe interface, calculated by two methods under different deposition conditions, 10 W with 20 mTorr for (a) and 50 W with 3 mTorr for (b). (c) Variation of resistivity as a function of the number of periods. The lines in (c) are guides for the eye.

Discussion. The superlattice structure can be considered as a configuration where Ir layers replace a portion of the Pt layers. Combining the results from ST-FMR and SP, the enhancement of ξ_{SOT} relative to Pt can be attributed to two distinct factors: the increase in θ_{SH} within the superlattice and the enhancement of T_{int} compared to Pt. For the rise in θ_{SH}, the lower resistivity of Ir compared to Pt results in reduced current density through the Pt

layer. Furthermore, since θ_{SH} of Ir is 0.038 or 0.045 (under different deposition conditions), which is lower than the values of 0.122 and 0.119 for Pt, this implies that the contribution of Ir to SOT would only account for approximately 25% in the superlattice if interfacial scattering is not considered. Therefore, one might expect the θ_{SH} of the superlattice to be lower than that of Pt when accounting solely for intrinsic and extrinsic contributions arising from impurities and defects within each layer. However, the observed enhancement in θ_{SH} indicates that the interfacial scattering plays a significant role in the extrinsic mechanism, thereby enhancing the overall value of θ_{SH}.

The increased resistivity in the superlattice is evidence of the strong interfacial scattering. Since the resistivity ρ of Ir is lower than that of Pt, if we solely consider scattering due to impurities and defects (neglecting interfacial scattering), the resistivity of superlattices should be lower than that of Pt. Moreover, superlattices with different periods would be expected to exhibit similar resistivity. Contrary to this expectation, we find that the resistivity of the superlattices is indeed higher than that of Pt. As the number of periods increases, the resistivity of the superlattices also rises, as shown in Fig. 5(c). This indicates a significant impact of interfacial scattering on the resistivity of the superlattice. [51]

We propose that the increased SOT efficiency may arise from the following processes. (1) Electrons are specularly scattered back into the Pt layer at the Ir/Pt interface, thereby increasing the probability of scattering events associated with impurities and defects. [30,51] (2) The differing environment at the Ir/Pt interface compared to the interior of the layer may result in skew scattering of electrons at these interfaces. [59–61]

Regarding the enhancement of T_{int}, it can be understood in terms of resistivity. Since the ρ of superlattices is higher than that of Pt, it leads to a smaller G_{NM} as compared to Pt. Because the $G_{eff}^{\uparrow\downarrow}$ of the superlattice samples and that of the Pt sample are almost the same, then according to the relationship $T_{int} = 2G_{eff}^{\uparrow\downarrow}/G_{NM}$, the T_{int} of the superlattice would be larger than that of Pt. As the number of periods increases, so does the resistivity. Given that T_{int} is proportional to resistivity, the observed increase in T_{int} within the superlattice is likely linked to the resistivity increase induced by interfacial scattering, which elucidates the overall enhancement in the superlattice.

Conclusion. In conclusion, to study the impact of interfacial scattering on SOT, we successfully constructed an Ir/Pt superlattice. XRD, STEM, and EDS measurements demonstrate the high crystalline quality and structure of the superlattices, indicating that defects- and impurities-related scattering in each Pt or Ir layer has been minimized in this experiment. Subsequently, ST-FMR and SP measurements were conducted to characterize the SOT, revealing varying degrees of enhancement in ξ_{SOT}, θ_{SH}, and T_{int}. Notably, for the low-power samples (10 W with 20 mTorr), ξ_{SOT} exhibits an average enhancement of 96.4% and a maximum enhancement of 120%, while θ_{SH} shows an average enhancement of 31.2% and a maximum enhancement of 44.8%. Through calculations and analysis, we prove that the superior performance of the superlattice in SOT can be attributed to additional scattering at the Ir/Pt interface. This interfacial scattering results in two significant effects. One is that it leads to a larger θ_{SH} in the superlattice compared to Pt. The other is that the increased resistivity caused by interfacial scattering contributes to a higher T_{int}. Both factors play a crucial role in enhancing ξ_{SOT}. We have highlighted the remarkable contribution of interfacial scattering to the SOT in epitaxial heavy metal superlattices. These findings may have important implications for the fields of spin manipulation and the development of spintronic devices in the future.

Acknowledgements. This work was financially supported by the Science Center of the National Science Foundation of China (Grant No. 52088101), the National Natural Science Foundation of China (Grant Nos. 52161160334, 12274437, 12174426, and 52271237), the Chinese Academy of Sciences (CAS) Project for Young Scientists in Basic Research No. YSBR-084, and the CAS Youth Interdisciplinary Team.

References

[1] Dyakonov M I and Perel V I 1971 *Phys. Lett. A* **35** 459
[2] Hirsch J E 1999 *Phys. Rev. Lett.* **83** 1834
[3] Zhang S 2000 *Phys. Rev. Lett.* **85** 393
[4] Sinova J, Culcer D, Niu Q, Sinitsyn N A, Jungwirth T, and MacDonald A H 2004 *Phys. Rev. Lett.* **92** 126603
[5] Kato Y K, Myers R C, Gossard A C, and Awschalom D D 2004 *Science* **306** 1910
[6] Valenzuela S O and Tinkham M 2006 *Nature* **442** 176
[7] Bychkov Yu A and Rashba É I 1984 *Sov. J. Exp. Theor. Phys. Lett.* **39** 78
[8] Miron I M, Garello K, Gaudin G, Zermatten P J, Costache M V, Auffret S, Bandiera S, Rodmacq B, Schuhl A, and Gambardella P 2011 *Nature* **476** 189
[9] Liu L, Lee O J, Gudmundsen T J, Ralph D C, and Buhrman R A 2012 *Phys. Rev. Lett.* **109** 096602
[10] Fukami S, Zhang C, DuttaGupta S, Kurenkov A, and Ohno H 2016 *Nat. Mater.* **15** 535
[11] Emori S, Bauer U, Ahn S M, Martinez E, and Beach G S D 2013 *Nat. Mater.* **12** 611
[12] Ryu K S, Thomas L, Yang S H, and Parkin S 2013 *Nat. Nanotechnol.* **8** 527
[13] Jiang W, Upadhyaya P, Zhang W, Yu G, Jungfleisch M B, Fradin F Y, Pearson J E, Tserkovnyak Y, Wang K L, Heinonen O, te Velthuis S G E, and Hoffmann A 2015 *Science* **349** 283
[14] Woo S, Litzius K, Krüger B, Im M Y, Caretta L, Richter K, Mann M, Krone A, Reeve R M, Weigand M, Agrawal P, Lemesh I, Mawass M A, Fischer P, Kläui M, and Beach G S D 2016 *Nat. Mater.* **15** 501
[15] Yu G, Upadhyaya P, Shao Q, Wu H, Yin G, Li X, He C, Jiang W, Han X, Amiri P K, and Wang K L 2017 *Nano Lett.* **17** 261
[16] Yu G, Jenkins A, Ma X, Razavi S A, He C, Yin G, Shao Q, He Q L, Wu H, Li W, Jiang W, Han X, Li X, Bleszynski Jayich A C, Amiri P K, and Wang K L 2018 *Nano Lett.* **18** 980
[17] Fukami S, Anekawa T, Zhang C, and Ohno H 2016 *Nat. Nanotechnol.* **11** 621
[18] Zhu L, Zhu L, Shi S, Ralph D C, and Buhrman R A 2020 *Adv. Electron. Mater.* **6** 1901131

[19] Wu H, Chen A, Zhang P, He H, Nance J, Guo C, Sasaki J, Shirokura T, Hai P N, Fang B, Razavi S A, Wong K, Wen Y, Ma Y, Yu G, Carman G P, Han X, Zhang X, and Wang K L 2021 *Nat. Commun.* **12** 6251

[20] Wan C, Zhang X, Yuan Z, Fang C, Kong W, Zhang Q, Wu H, Khan U, and Han X 2017 *Adv. Electron. Mater.* **3** 1600282

[21] Zhang X, Wan C H, Yuan Z H, Fang C, Kong W J, Wu H, Zhang Q T, Tao B S, and Han X F 2017 *J. Magn. Magn. Mater.* **428** 401

[22] Luo Z, Hrabec A, Dao T P, Sala G, Finizio S, Feng J, Mayr S, Raabe J, Gambardella P, and Heyderman L J 2020 *Nature* **579** 214

[23] Demidov V E, Urazhdin S, Ulrichs H, Tiberkevich V, Slavin A, Baither D, Schmitz G, and Demokritov S O 2012 *Nat. Mater.* **11** 1028

[24] Liu L, Pai C F, Ralph D C, and Buhrman R A 2012 *Phys. Rev. Lett.* **109** 186602

[25] Liu R H, Lim W L, and Urazhdin S 2013 *Phys. Rev. Lett.* **110** 147601

[26] Awad A A, Dürrenfeld P, Houshang A, Dvornik M, Iacocca E, Dumas R K, and Åkerman J 2017 *Nat. Phys.* **13** 292

[27] Guo G Y, Murakami S, Chen T W, and Nagaosa N 2008 *Phys. Rev. Lett.* **100** 096401

[28] Zhu L, Ralph Daniel C, and Buhrman R A 2018 *Phys. Rev. Appl.* **10** 031001

[29] Zhu L, Zhu L, Sui M, Ralph D C, and Buhrman R A 2019 *Sci. Adv.* **5** eaav8025

[30] Zhu L, Zhu L, Shi S, Sui M, Ralph D C, and Buhrman R A 2019 *Phys. Rev. Appl.* **11** 061004

[31] Zhu L, Sobotkiewich K, Ma X, Li X, Ralph D C, and Buhrman R A 2019 *Adv. Funct. Mater.* **29** 1805822

[32] Zhu L and Buhrman R A 2019 *Phys. Rev. Appl.* **12** 051002

[33] Wang Y, Zhu D, Wu Y, Yang Y, Yu J, Ramaswamy R, Mishra R, Shi S, Elyasi M, Teo K L, Wu Y, and Yang H 2017 *Nat. Commun.* **8** 1364

[34] Shi S, Wang A, Wang Y, Ramaswamy R, Shen L, Moon J, Zhu D, Yu J, Oh S, Feng Y, and Yang H 2018 *Phys. Rev. B* **97** 041115

[35] Wu H, Zhang P, Deng P, Lan Q, Pan Q, Razavi S A, Che X, Huang L, Dai B, Wong K, Han X, and Wang K L 2019 *Phys. Rev. Lett.* **123** 207205

[36] Wu H, Xu Y, Deng P, Pan Q J, Razavi S A, Wong K, Huang L, Dai B Q, Shao Q M, Yu G Q, Han X F, Rojas-Sánchez J C, Mangin S, and Wang K L 2019 *Adv. Mater.* **31** 1901681

[37] Cui B, Chen A, Zhang X, Fang B, Zeng Z, Zhang P, Zhang J, He W, Yu G, Yan P, Han X, Wang K L, Zhang X, and Wu H 2023 *Adv. Mater.* **35** 2302350

[38] MacNeill D, Stiehl G M, Guimaraes M H D, Buhrman R A, Park J, and Ralph D C 2017 *Nat. Phys.* **13** 300

[39] Guimarães M H D, Stiehl G M, MacNeill D, Reynolds N D, and Ralph D C 2018 *Nano Lett.* **18** 1311

[40] Xu H, Wei J, Zhou H, Feng J, Xu T, Du H, He C, Huang Y, Zhang J, Liu Y, Wu H C, Guo C, Wang X, Guang Y, Wei H, Peng Y, Jiang W, Yu G, and Han X 2020 *Adv. Mater.* **32** 2000513

[41] Bainsla L, Zhao B, Behera N, Hoque A M, Sjöström L, Martinelli A, Abdel-Hafiez M, Åkerman J, and Dash S P 2024 *Nat. Commun.* **15** 4649

[42] Liu L, Pai C F, Li Y, Tseng H W, Ralph D C, and Buhrman R A 2012 *Science* **336** 555

[43] Wang Y, Deorani P, Qiu X, Kwon J H, and Yang H 2014 *Appl. Phys. Lett.* **105** 152412

[44] Sui X, Wang C, Kim J, Wang J, Rhim S H, Duan W, and Kioussis N 2017 *Phys. Rev. B* **96** 241105

[45] Liu L, Moriyama T, Ralph D C, and Buhrman R A 2011 *Phys. Rev. Lett.* **106** 036601

[46] Pai C F, Ou Y, Vilela-Leão L H, Ralph D C, and Buhrman R A 2015 *Phys. Rev. B* **92** 064426

[47] Nguyen M H, Pai C F, Nguyen K X, Muller D A, Ralph D C, and Buhrman R A 2015 *Appl. Phys. Lett.* **106** 222402

[48] Zhang W, Han W, Jiang X, Yang S H, and Parkin S S P 2015 *Nat. Phys.* **11** 496

[49] Fuchs K 1938 *Math. Proc. Camb. Philos. Soc.* **34** 100

[50] Sondheimer E H 1952 *Adv. Phys.* **1** 1

[51] Shen P and Gall D 2024 *J. Appl. Phys.* **136** 075305

[52] Nguyen M H, Ralph D C, and Buhrman R A 2016 *Phys. Rev. Lett.* **116** 126601

[53] Asthagiri A, Niederberger C, Francis A J, Porter L M, Salvador P A, and Sholl D S 2003 *Surf. Sci.* **537** 134

[54] Ito M, Sawada K and Ishida M 2007 *Solid State Phenom.* **124** 181

[55] Wei J, Zhong H, Liu J, Wang X, Meng F, Xu H, Liu Y, Luo X, Zhang Q, Guang Y, Feng J, Zhang J, Yang L, Ge C, Gu L, Jin K, Yu G, and Han X 2021 *Adv. Funct. Mater.* **31** 2100380

[56] Zhang Q, Zhao Y, He C, Huo Y, Cui B, Zhu Z, Zhang G, Yu G, He B, Zhang Y, Lyu H, Guo Y, Qi J, Shen S, Wei H, Shen B, and Wang S 2022 *Adv. Electron. Mater.* **8** 2200845

[57] Dong J, Cheng C, Wei J, Xu H, Zhang Y, Wang Y, Zhu Z, Li L, Wu H, Yu G, and Han X 2023 *Appl. Phys. Lett.* **122** 122401

[58] Sun R, Li Y, Xie Z K, Li Y, Zhao X T, Liu W, Zhang Z D, Zhu T, Cheng Z H, and He W 2020 *J. Magn. Magn. Mater.* **497** 165971

[59] Shumilin A V and Kabanov V V 2023 *Phys. Rev. Res.* **5** 033215

[60] Zhang J Y, Dou P W, Liu R Y, Wang Y B, Deng X, Feng L Y, Zheng X Q, Huang H, and Wang S G 2023 *Appl. Phys. Lett.* **123** 182401

[61] Singh D and Senthil Kumar M 2024 *J. Magn. Magn. Mater.* **596** 171975